Large thermopower in topological surface state of Sn-BSTS topological insulators: Thermoelectrics and energy-dependent relaxation times

Stephane Yu Matsushita, Kakeru Ichimura, Khuong Kim Huynh, and Katsumi Tanigaki

Phys. Rev. Materials **5**, 014205 — Published 25 January 2021

DOI: 10.1103/PhysRevMaterials.5.014205

Large thermopower in topological surface state of Sn-BSTS topological insulators: Thermoelectrics and Energy-dependent Relaxation Times

Stephane Yu Matsushita,[1*] *Kakeru Ichimura*[1], *Khuong Kim Huynh,*[2] *Katsumi Tanigaki*[1, 2, 3**]

[1]Department of Physics, Graduate School of Science, Tohoku University, Sendai 980-8578, Japan

[2]WPI-Advanced Institute for Materials Research, 2-1-1 Katahira, Aoba-ku, Sendai, Miyagi, 980-8578, Japan

[3]Beijing Academy of Quantum Information Sciences (BAQIS)

Bld.#3 No.10, Xibeiwang East Rd., Haiden District, Beijing 100193、China

*E-mail address: *m.stephane@tohoku.ac.jp

, **tanigaki@tohoku.ac.jp

Key words: topological insulator, thin film, thermoelectric transport, power factor

Abstract

Topological surface Dirac states (TSDSs) generated in three-dimensional topological insulators (3D-TIs) are currently of significant interest for new science and advanced technologies. In contrast to many other thermoelectric materials, 3D-TIs exhibit a significant potential to achieve a large enhancement in thermoelectric power factor ($PF = \sigma S^2$) due to their special topological symmetry. However, only limited experiments and discussions have been made so far for elucidating the thermoelectric properties of TSDS. Herein, we report a large *S* and *PF* observed for high-quality single-crystal flakes of Sn-$Bi_{1.1}Sb_{0.9}TeS_2$ (Sn-BSTS). Accurate interpretations that the energy dependent relaxation times $\tau(E)$ play an important role in thermoelectrical transport of 3D-TIs are provided. Among 3D-TIs, Sn-BSTS has the highest bulk insulation and shows intrinsic TSDS transport without bulk contributions, along with its hallmark of quantum integer Hall effect at high temperatures. Based on the longitudinal/transverse electrical transport and the thermoelectric coefficient, $\tau(E) \propto E^{0.21}$ is accurately deduced. As a consequence of the energy-dependent $\tau(E)$, a

large enhancement in both S and PF is obtained (S=58 μVK^{-1} and PF=5.0 mWm^{-1}K^{-2} at 77 K), leading to a large increase of 160% for S and 280% for PF when compared to those of Graphene at 77 K. The potential thermoelectric performance of the pure TSDS is discussed based on the Boltzmann transport equations.

Main text

1. Introduction

Numerous theoretical and experimental studies to develop highly efficient thermoelectrics (TE) have been carried out by utilizing phonons [1,2] to control thermal conductivity. However, limited approaches to enhance the efficiency of TE have been performed by modifying the electronic states, e.g., the density of states (DOS) at the Fermi level [3,4] or electron correlations [5,6]. In the latter approaches, although the relaxation times (τ(E)) of electrons associated with energy dependence upon the scattering mechanism are generally important, they have frequently been neglected in the design of TE materials. According to the non-equilibrium Boltzmann transport theory, TE factors such as thermopower S and power factor $PF = \sigma S^2$ (σ: electrical conductivity) are related to the derivative of the spectral conductivity $\sigma(E)$ with respect to the energy (E). Hence, a material that has an E-dependent $\tau(E)$ may exhibit enhanced values of S and PF, which are greater than those observed in conventional TE materials [5,6].

Three-dimensional topological insulators (3D-TIs) are one of such systems as they are considered to exhibit a strongly E-dependent $\tau(E)$ value, which arises from the 1:1 correspondence between the surface and the bulk. This characteristic positions 3D-TIs as potential candidates for application of high-performance TE materials [6,7]. 3D-TIs provide intriguing helical massless Dirac fermions on a two-dimensional (2D) topological surface Dirac states (TSDSs) generated on an insulating bulk [8,9]. The unique TSDSs, which are topologically non-trivial and protected by time-reversal symmetry, give rise to a strong prohibition of backward scatterings; this leads to the formation of channels ideal for fast and ultralow-dissipative electrical transport.

The E-dependence of $\tau(E)$, and therefore the scattering mechanism of the Dirac electrons, is currently discussed in several theoretical works. Nomura et al., described the scattering mechanism in the aspect of long-range coulomb scattering (LCS) and short-range delta scattering (SDS), which gives $\tau(E) \propto E$ and $\tau(E) \propto E^{-1}$, respectively. When the Fermi energy (E_F) locates near the neutral Dirac point (NDP), LCS becomes dominant and the relaxation time approaches to the limit of

$\tau(E) \propto E$. In this situation, two times larger S and four times larger PF are expected based on the Motto relation, which is described later in the discussion part. Another aspect is the bulk-surface coupling near the bulk band edge proposed by Saha et al.[10] They calculated the disorder- and phonon-induced coupling between the TSDS and the bulk state in 3D-TIs, and found that $\tau(E)$ of TSDS is extremely suppressed near the bulk band edge due to the bulk-surface coupling. Xu et al.[6] calculated the thermopower of TSDS in the bulk band edge region with using a dual τ model, and proposed an anomalous Seebeck effect due to the anomaly of τ.

Several pioneering studies of the thermoelectrics of Dirac electrons have been reported for graphene (Gr) [5,13,14]. As a result of the high carrier mobility of topologically protected Dirac electrons, Gr is reported to show the largest *PF* among the 2D TE materials thus far. This is because the scattering mechanism of itinerant electrons to be separated from the impurities existing on a substrate can be controlled by inserting an inert BN intermediate layer [5]. However, compared to Gr, far few studies have been reported on 3D-TIs and discussions on the TE properties of these materials and firm experimental confirmation of *E*-dependent $\tau(E)$ have been limited [6,7,10,17].

Here, we report that *E*-dependent $\tau(E)$ is essential for the TE properties of 3D-TIs. An evident experimental confirmation is provided by the simultaneous observations of the integer quantum Hall effects (IQHE) and Shubnikov-de Haas (SdH) quantum oscillations together with TE transports, which were achieved by employing high-quality single-crystal flakes of Sn-doped $Bi_{1.1}Sb_{0.9}Te_2S$ (hereafter named Sn-BSTS). The accurate band picture required for unambiguous interpretations of TE properties is derived from the experimental observations of IQHE and SdH. A large enhancement in both S and PF was obtained (S=58 μVK^{-1} and PF=5.0 $mWm^{-1}K^{-2}$ at 77 K), leading to a large increase of 160% for S and 280% for PF when compared to those of Gr. The reasons for the highly efficient TE are shown in terms of the *E*-dependence of $\tau(E)$ in the framework of the non-equilibrium Boltzmann transport theory based on the accurate band picture. Our present work focusing on TE of TSDSs provides an important contribution to the continuing recent debate as to whether high TE efficiency can be realized in 3D-TIs.

2. Experimental

Single crystals of Sn-BSTS were synthesized by melting high-purity elements, Bi (5N), Sb (5N) , Te (5N) , S (5N), and Sn (5N), and characterized by EDX and XRD as reported elsewhere [21]. The samples were exfoliated from a piece of the bulk crystal by using a sheet of double-sided tape and transferred on a sample plate followed by being subjected to electrical transport measurements All electrical transport measurements were carried out using Physical Properties Measurement System (PPMS, Quantum Design) under a magnetic field (B) in the temperature (T) range from 300 K to 2 K.

3. Results

3.1. Sheet resistance of Sn-BSTS flakes

The energy gap of 3D-TIs is engineered using the concept of charged defect control, which has been investigated in numerous studies on the tetradymites of V^{th} (Sb,Bi)-VI^{th} (Se,Te) elements [16-21]. We reported recently that the highest quality of TSDSs among the tetradymite 3D-TIs can be achieved experimentally in high-quality single-crystal Sn-BSTS flakes, which are prepared using the Scotch-tape exfoliation technique [21]. Sn-BSTS has a crystal structure (Fig. 1a), which is similar to that of $Bi_{2-x}Sb_xTe_{3-y}Se_y$ (BSTS) except for the center site of the unit cell wherein sulfur (S) is incorporated in place of selenium (Se). This results in an increase in the bulk band gap with high bulk insulation that is caused by the large electronegativity of sulfur [20,21].

The temperature (T) dependence of the sheet resistance ($R_{\square}$) of Sn-BSTS with thicknesses (t) of 113, 26, 7, and 3 μm is shown in Fig. 1(b). The thickest flake (t = 113 μm) showed an insulating/semiconducting T-dependence, which is a typical characteristic of a 3D-TI bulk. With decreasing T, $R_{\square}$ increased initially and saturated at 120 K; it decreased further as T was further lowered due to the metallic property of the TSDS. As the flake thickness decreased, the bulk contribution decreased and consequently the saturation temperature increased with decreasing the

flake thickness. This observation indicated that the excitation of bulk carriers can effectively be suppressed to ensure that the surface transport is dominant even at high *T*s.

Figure 1(c) shows the ratio of the sheet conductance of the surface (G_s) to the total sheet conductance (G_{tot}) as a function of thickness (t) and temperature (T). The value of G_s/G_{tot} was determined by fitting the sheet resistance of samples with a parallel circuit model consisting of the bulk and surface channels described as $R_{\square} = \frac{1}{G_{tot}} = \frac{1}{G_b+G_s}$ with $G_b = \frac{t}{\rho_{b0}e^{\Delta/kT}}$ and $G_s = \frac{1}{R_{sh0}+AT}$, where k is the Bolzmann constant with fitting parameters; the bulk channel consists of ρ_{b0} and Δ corresponding to the high temperature bulk resistivity and the activation energy, respectively, and the surface channel consists of R_{sh0} and A representing the low-T residual resistance and the electron-phonon scattering, respectively [21,22] (See supplemental for the detail). Analyses of the experimental results gave Δ of 140 ± 10 meV, which is three times larger than that of BSTS [22]. The thinnest sample (t = 3 μm) showed the surface dominant transport (G_s/G_{tot} > 80%) up to 210 K.

3.2. Seebeck coefficient of Sn-BSTS flakes

Since the carrier type of Sn-BSTS is hole for the bulk channel, while it is electron for the surface channel [20], the polarity of the Seebeck coefficient (S) of the bulk and the surface carriers is opposite. Therefore, the surface dominant transport responsible for the electric conductance can be seen more clearly in thermopower (S), in terms of sign change in S, as shown in Fig. 2. The thickest flake (113 μm) showed a positive value of S with a nonlinear T dependence, where a maximum value of S = 651 μV K^{-1} was observed with positive sign at T_{max} = 227 K, while it changes to negative at T_c = 101 K. These experimental results indicate that the dominant carriers change from holes to electrons with a decrease in T. Non-linear T dependence of S is frequently observed in semiconductors when hole carriers are generated in a bulk band via thermal excitations of electrons trapped in a shallow impurity level[7,15]. With a reduction in film thickness (t), both T_{max} and T_c

shifted to higher *T*s and the positive component of *S* gradually diminished, indicating that the contribution of the bulk carriers is greatly suppressed in Sn-BSTS. In the case of the thinnest flake of 3 μm, a *T*-linear *S* with a negative sign was clearly observed below ca. 150 K and the metallic Dirac electrons of TSDSs become dominant in the electrical transport.

3.3. Hall resistivity of Sn-BSTS flakes

The experimental observations of half-integer quantum Hall effect (HI-QHE) can be an important hallmark for confirming the pure and intrinsic electrical transport on TSDS. Figure 3 shows the Hall resistance (R_{yx}) of the four Sn-BSTS flakes at 2 K as a function of magnetic field (B). For the thick flakes of 113 and 26 μm, R_{yx} shows a typical nonlinear shape, being indicative of a multi-channeled transport of both high mobility electrons on the topological surface and low mobility holes in the bulk. On the other hand, with a decrement in thickness to 7 μm, R_{yx} started to show weak oscillations and saturated at above 6 T with the quantized value of $R_{yx}=h/e^2$. The oscillations of R_{yx} became more visible for the 3 μm -flake, where the clear quantized plateaus were observed at $R_{yx}=h/2e^2$ and h/e^2, correspond to the integer Hall conductance at $\sigma_{xy}=2e^2/h$ and e^2/h of QSHE in 3D-TIs. These experimental observations are the firm fact that the pure TSDS electrical transport is achieved in the μm-thick flakes [21].

3.4. SdH oscillations of Sn-BSTS flakes

Typical SdH oscillations of Sn-BSTS flakes with 7 μm-flake are shown in Figure 4 (a). Clear oscillations were observed as a function of 1/B and the two specific SdH frequencies (B_F) of $B_F = 2.2$ T and 5.5 T were deduced by the fast Fourier transform (FFT). The fan diagrams of the oscillatory components of 1/B were plotted as a function of the quantum number of N for each B_F value, and β = 0.69 (BF=2.2 T) and 0.65 (BF=5.5 T) were evaluated as shown in Fig.4(b). Both electronic states

have β values close to 0.5 as the intercept, indicating that both states are the non-trivial TSDSs. By applying the relationships of $n_{2D} = \frac{2S_F}{\pi^2} = \pi k_F^2/(2\pi)^2$ (the 2D carrier density (n_{2D}), the Fermi vector (k_F) and the 2D Fermi surface area ($\boldsymbol{S_F}$)), the value n_{2D} can be evaluated as $n_{2D} = 5.3 \times 10^{10}$ cm^{-2} and 1.3×10^{11} cm^{-1}, respectively. These values are similar to $n_{2D} = 5.6 \times 10^{10}$ cm^{-2} for the bottom surface and $n_{2D} = 1.6 \times 10^{11}$ cm^{-2} for the top surface of the 3 μm-flake as reported elsewhere [21].

4. Discussion

4.1. Band picture of Sn-BSTS flakes

The sheet resistance, the thermopower, and the QSHE described earlier clearly indicate the fact that the contribution of bulk carriers in electrical transport is negligibly small at low-*T*s for both the 3 μm and the 7 μm Sn-BSTS flakes. In order to discuss the TE properties of the TSDS, we, first, evaluated the accurate band picture of the 3 μm and the 7 μm Sn-BSTS flakes as shown in Figure 5(a), based on the measurements of QSHE and SdH [21]. The Fermi velocity v_F, corresponding to the gradient of the linear dispersion of Dirac band, was estimated to be 4.8×10^5 ms^{-1}. The position of E_F from the NDP (E_t: top surface, E_b: bottom surface) was evaluated to be $E_t = 44$ meV and 40 meV for the 3 and the 7 μm-flake, respectively, and $E_b = 26$ meV was the same for the both flakes. Since the bulk state and the two TSDSs are connected continuously, we estimated the chemical potential (μ) of the bulk state as the average of the two TSDSs of the top and bottom surfaces to be $\mu = 35$ meV (33 meV) away from the NDP for the 3 μm (7 μm) flake. The level of NDP can be estimated to be 120 meV away from the valence band top (VBT) by employing the ARPES observations by Kushwaha et al.[20]. The position of μ from the VBT, (120 + μ) meV, agree well with the activation energy (Δ=140 $\pm$ 10 meV) determined from the analysis of sheet resistance measurements.

4.2. TE transport of TSDS: Energy dependent relaxation time

Taking into account the contribution of both top and bottom TSDS, the thermoelectric transport of Sn-BSTS can be described as a parallel conductive channel circuit composed of the two topological surfaces well separated via a highly insulating bulk layer as shown in Fig. 5(b). The total thermopower S_{tot} can consequently be described by

$$S_{\mathrm{tot}} = \frac{G_{\mathrm{t}}S_{\mathrm{t}}+G_{\mathrm{b}}S_{\mathrm{b}}}{G_{\mathrm{t}}+G_{\mathrm{b}}} \qquad (1)\,,$$

where G_{t} (G_{b}) and S_{t} (S_{b}) are the sheet conductance and the thermopower of the top (bottom) surface, respectively. Since both TSDSs are the metallic states, the Mott formula can be applied to describe S as

$$S = \frac{\pi^2 k_B^2}{3e}\,\frac{T}{\sigma(\mu)}\,\frac{\partial\sigma(E)}{\partial E}\Big|_{E_F} \qquad (2),$$

where $\sigma(E)$ is the energy-dependent conductivity expressed by $\sigma(\varepsilon) = e^2 v_F^2 D(E)\tau(E)/2$ with the Fermi velocity v_F, the density of states (DOS) $D(E)$, and the energy-dependent relaxation time $\tau(\propto E^{\gamma})$. The linear dispersion of the Dirac band gives the DOS of the surface 2D-TSDS fermions described as $D(E) = g|E|/2\pi\hbar^2 v_F^2$, where g is the degeneracy (g=4 for Graphene and g=1 for 3D-TI). Therefore, S of a TSDS can be formulated as

$$S = \frac{\pi^2 k_B}{3e}\,\frac{k_B T}{E_F}\,(\gamma+1) \qquad (3).$$

The sheet conductance of each surface can be determined using the experimental data of total sheet conductance, G_{tot}, with the ratio of conductance between the two surfaces being $(en\mu)_{top}:(en\mu)_{bottom} = 0.63:0.37$, which is obtained by analyzing the SdH oscillations for the 3 μm-flake [21]. Consequently, only the power index "γ" of $\tau(E)$ is left as the unknown parameter, which can be determined by fitting the experimental data with eq. (3). As shown in Fig. 5(c), S for the 3 μm-flake gave an excellent agreement with a value of $\gamma = 0.21$. A similar analysis of the 7 μm-flake gave a comparable value of $\gamma = 0.22$ as shown in Fig. 5(d). These values of γ indicate that the relaxation time (τ) of 3D-TIs is E-dependent.

4.3 Estimation of the Power factor of TSDS

(i) Power factor of TSDS of Sn-BSTS at low T: Estimation from experimental results

In order to discuss the TE properties of TSDSs, we conducted further analyses for the 3 μm-flake. We start with the discussion of *PF* at low-*T*s, where the surface dominant transport is realized and therefore *PF* of TSDS can be estimated directly from the experimental data. For instance, the sheet conductance and the thermopower of the 3 μm flake were $G_s = 2.4 \times 10^{-4}$ S and $S = 57.7$ μVK^{-1} at 77 K, respectively. In the case of 2D TE materials, such as Graphene [5], the sheet conductance G is converted to the conductivity σ by using the thickness of monatomic layer in order to compare PF with those of 3D materials. In this framework, the PF of TSDS of 3 μm-flake was estimated to be 5.0 mWm^{-1}K^{-2} at 77 K. This value is 2.8 times greater than that of graphene at the same temperature, PF=1.8 mWm^{-1}K^{-2} reported by Duan et al. for Gr/hBN[5].

The *PF* of Sn-BSTS as a function of *T* up to 200 K, calculated from the above framework, was shown in Fig. 7 as the red balls. The value of *PF* increased as a function of *T* but saturated above 150 K due to the contribution of bulk carriers excited at high *T*s. It is important to know the fact that the *PF* value of the pure TSDS at 77 K was already comparable to those of other 2D and 3D TE materials recorded at around 300 K[3-5,23-32]. According to the previous work on the BSTS thin films [7,15], the pure TSDS has metallic properties and the thermopower *S* and *PF* monotonically increase with *T*. Therefore, a much larger value of PF could be expected in the pure TSDS at high-T region.

(ii) Power factor of TSDS of Sn-BSTS at high T: Deconvolution of TSDS and Bulk TE

In order to estimate the potential magnitude of the PF of pure TSDS of Sn-BSTS, we tried to deconvolute the surface and the bulk contribution in TE transport of Sn-BSTS. Since the E_F locates

near to the NDP and far from the bulk band edge, the surface-bulk interaction of the electrons in TSDS can be considered to be very small. Therefore, it is possible to regard the surface and the bulk channel as the separated ones. Applying the equation (1) for the bulk and the surface channel, the product $(GS)_{\mathrm{tot}}$ of the observed sheet conductance and the thermopower is described as

$$(GS)_{\mathrm{tot}} = G_{\mathrm{surf}}S_{\mathrm{surf}} + G_{\mathrm{bulk}}S_{\mathrm{bulk}} \quad (4)$$

with the sum of the surface and the bulk terms. Here, the surface term can be determined from the sheet conductance of the surface *G*s (Sec. 3.1 and Supplemental Sec. S1) and the Mott equation (1) for S (Sec. 4.2). The bulk term was calculated using the Boltzmann transport equation as

$$G_{bulk} = d\sigma_{bulk} = de^2L_0,$$
$$S_{bulk} = -\frac{1}{eT}\frac{L_1}{L_0}, \quad (5)$$
$$L_n = c_b(k_BT)^{1+n}\int_{\Delta}^{\infty} dx \frac{x^2-{\Delta_B}^2}{x}\left[\frac{(x-\mu)^n}{\cosh^2\frac{x-\mu}{2}} + \frac{(-x-\mu)^n}{\cosh^2\frac{x+\mu}{2}}\right],$$

where d is the thickness of the flake, Δ_B the activation energy of the bulk, μ the chemical potential, and $c_b = \frac{\mu^*}{\pi^2 e}\left(\frac{2m^*}{\hbar^2}\right)^{3/2}$ with the carrier mobility μ^* and the effective mass m^*. The values of Δ_B and μ were estimated based on the band picture shown in Fig. 5(a), and the other parameters were estimated by fitting the sheet resistance of the 3 μm-flake with eq.(5) (See supplemental for the analysis details). The calculated $(GS)_{\mathrm{tot}}$ agrees well to the experimental value as shown in Fig. 6.

According to the deconvolution analyses described above, we extend the discussion of *PF* to 300 K. The deconvoluted *PF* of the TSDS, which is shown as a dashed red line in Figure 7, was in reasonable agreement with the total *PF* of Sn-BSTS (red balls) up to 80 K; this indicates that TSDSs dominate the TE transport at low *T*s for Sn-BSTS. *PF* of the pure TSDS is expected to reach $PF = 60.0$ mWm^{-1}K^{-2} at 300 K through extrapolation.

While the PF (electronic term in TE properties) of Sn-BSTS can be estimated in the framework of 2D-TE materials, the value of κ (the thermal term in TE properties) is not straight forward, since the phonon term is involved in addition to electronic one for the general

measurements. In general discussions, electronic transport of TSDS predominantly occurs with less backward scatterings through topologically protected 2D conduction channels of the nontrivial electronic bands, while thermal energy flows with being assisted by both electric and phononic channels and therefore becomes more 3D-like nature given the longer mean-free path of phonon dispersions. For improved fundamental understanding, more careful discussions will be required in the future.

4.4. Relation to Scattering mechanism and TE performance: 3D-TI v.s. Graphene:

Our present analyses allow detailed and valid comparisons between 3D-TIs and Gr in terms of *S* and *PF*. Figure 8(a) and (b) show *S* and *PF* of the pure TSDSs of Sn-BSTS evaluated earlier (red), and two types of Gr systems: Gr on a SiO_2/Si substrate (black) and Gr on a hexagonal boron nitride (hBN) substrate (blue). The PF of Gr as a TE material was demonstrated to be the highest among the 2D materials studied so far (Duan et al [5]). Sn-BSTS, Gr/SiO_2/Si, and Gr/hBN/SiO_2/Si show similar trends of enhancement in *S* and *PF* as a function of *T*. Since a clear enhancement in these parameters is evident when the structure was changed from Gr/SiO_2/Si to Gr/hBN/SiO_2/Si where a high quality insulator of hBN is inserted between Gr and SiO_2, the reason of the observed improvement is considered to be associated with a good insulator between a 2D Dirac layer and a substrate, and such an understating will further be extended to the situation encountered for Sn-BSTS.

According to the Eq. (3), the enhancement in *S* and *PF* is related to the power index term, γ of energy E, and such an enhancement becomes greatly important when the relaxation time τ(E) is strongly energy-dependent [5-7,33] as discussed here. The parameter of γ in τ(E) is associated with the scattering mechanism of transporting carriers. In the case of a Dirac system such a Gr, a long-range coulombic scattering (LCS) is theoretically considered become dominant at low *Ts* when the E_F is close to the NDP [11,12,33]. The disordered potential of LCS is described as $V(\boldsymbol{r}) = \sum_I^{N_i} e^2/\epsilon|\boldsymbol{r} - \boldsymbol{R_I}|$ with the dielectric constant ϵ, and $\tau \propto E$ ($\gamma = 1$). Consequently, a large value of S is expected

for an ideal 2D Dirac system such as a free-standing Gr sheet away from a substrate, which can be twice larger than those of the conventional materials. When Gr is placed on a SiO_2/Si substrate, however, charge impurities existing in a SiO_2 insulating substrate would generate potential fluctuations in $V(\boldsymbol{r})$ so that LCS could be rendered to be $\gamma \ll 1$, as shown in Figure 8(c).

A schematic comparison between Gr/hBN/SiO_2/Si and 3D-TI is shown in Figure 8(c). In the above scenario, as the concentration of the charge impurities on the interface increases, the value of PF will decrease. Duan et al. [5] succeeded to minimize the effects by inserting a layer of hBN between SiO_2 and Gr, the latter of which becomes insensitive and free from the trapped charges on a substrate. The concentration of the charge impurities was estimated to be $n_{2D} = 0.3 \times 10^{12}$ cm^{-2} for the Gr/SiO_2 interface, and $n_{2D} = 0.2 \times 10^{12}$ cm^{-2} for Gr/hBN interface, in their report. In the case of our Sn-BSTS, the concentration of the charge impurities can be estimated from the carrier density of the bulk state. According to the two-carrier model fitting of the Hall resistivity at 300 K, the carrier concentration of the bulk was $n_{3D} = 1.02 \times 10^{18}$ cm^{-3}. Assuming that the depth of the impurities affects on the potential fluctuation as d=1 nm (same as Duan et al.), the charge impurities in the bulk-surface interface is estimated as $n_{2D} = 0.1 \times 10^{12}$ cm^{-2}, which is smaller than that of Gr/hBN. Therefore, 3D-TIs (TSDS/Insulator/TSDS) could become an ideal structure surpassing the performance of Gr/hBN/SiO_2/Si. Consequently, the ideal LCS transport of TSDSs gives the value of γ toward +1 and an increase in the *S* and *PF* values. In addition, S and PF values of 3D-TIs could become twice as large as those of Gr/hBN/SiO_2/Si as a consequence of top and bottom TSDSs.

4.5 Comparison among 3D-TIs: Sn-BSTS vs BSTS

It is worthwhile to compare the present results of Sn-BSTS to those of other 3D-TIs. Here, we make a comparison between Sn-BSTS and BSTS reported in ref [7]. In the previous study, the TE properties on TSDS was explained for BSTS thin films prepared by a physical vaper phase growth method. The bulk contribution was able to be suppressed by decreasing the film thickness, and the surface dominant electrical transport and thermopower were observed in the BSTS thin film.

While the qualitative behavior of the TE properties of BSTS is consistent with those of Sn-BSTS described in the present study, two critical differences are pointed out with each other.

First, the critical thickness, where the bulk transport is suppressed and the good surface dominant transport is realized, was greatly improved in Sn-BSTS. The thermoelectric transport parameters ($R_{\square}$ and S) on the TSDS became dominant in the thickness of μm-scale in Sn-BSTS, while they were only observed in the thickness of nm-scale in BSTS. This difference can be understood in terms of the difference in the intrinsic insulating property of the bulk state. Sn-BSTS has a bulk band gap of around 0.35 eV, which is larger than that of BSTS of around 0.3 eV. Therefore, the Sn-BSTS is greatly more insulating than BSTS, which enables the surface dominant transports in the thicker film thickness. The critical thickness of Sn-BSTS, to be defined as the thickness where the surface conductivity ratio becomes G_s/G_{tot}=80% at 300 K, can be estimated as tc=0.4 μm, from the results of fitting analysis in the supplemental.

The second factor is the power index γ of the relaxation time. The value of γ was estimated to be γ=0.21 in Sn-BSTS. On the other hand, in the case of BSTS, γ was estimated to be γ=-0.6. This negative value of γ is close to the limit of γ=-1, corresponding to the short-range neutral impurity scattering (or phonon scattering). This difference can be considered by the following two point of views. One is the potential fluctuations arising from the bulk carriers. Since the BSTS films have the larger bulk carrier density than that of Sn-BSTS, the magnitude of the potential fluctuations could be larger, plausibly leading to a reduction in γ from unity. The other is the position of E_F. In the case of BSTS, the E_F resides at 59 meV above the NDP, being far apart from the NDP compared to that of the Sn-BSTS flake. As was noted in the theoretical study [33], the value of γ becomes to +1 by approaching to the NDP, while it becomes to -1 by approaching to the edge of bulk band. Therefore, γ will be smaller by leaving the E_F apart from the NDP.

Taking the above discussions into account, three parameters would be the kyes in order to elevate the TE properties of 3D-TIs: bulk band gap, film thickness, and the position of E_F. Up to now, Sn-BSTS has the largest bulk band gap, and further improvements of PF can be expected by

decreasing the thickness of the flack to 0.4 μm and tuning the E_F closer to the NDP. The latter will be possible by a gating technique in electronic transistors or tuning the doping level of the Sn atoms.

5. Conclusions

In summary, we performed electrical transport measurements by focusing on the TE of high-quality single-crystal Sn-BSTS flakes. Because of the high electrical insulation of the bulk for Sn-BSTS, the contribution of the bulk carriers via thermal excitations was significantly suppressed, even in thick films in the μm scale. We determined the accurate band picture of both top and bottom TSDSs using IQHE and SdH and made unambiguous interpretations of the strong *E*-dependent relaxation times ($\tau(E) \propto E^{\gamma}$) within the framework of Boltzmann transport theory. As a consequence of the strong E-dependence in $\tau(E)$ originating from topologically constrained one-to-one correspondence between bulk and top/bottom TSDSs, the S and the PF values of TSDSs of 3D-TIs were significantly superior to those of Gr reported so far. A further reduction of the bulk transport by reducing the film thickness as well as tuning of the fermi energy close to the NDP can enhance the PF of the pure TSDS to be a good candidate for highly efficient TE-materials.

Acknowledgements

The authors thank T. Chiba for valuable discussions on the theoretical aspects of relaxation times. This work was supported, in part, by a Grant-in-Aid for Scientific Research from the Ministry of Education, Culture, Sports, Science and Technology (MEXT), JSPS KAKENHI Grants (No. 17K14329, 18H04471, 17-18H05326, 18H04304, 18H03883, and 18H03858) and thermal management of CREST, JST. This work was also sponsored by research grants from The Iwatani Naoji Foundation's Research Grant. The authors also received support from the World Premier International Research Center Initiative (WPI), MEXT, Japan.

References

[1] B. C. Sales, D. Mandrus, R. K. Williarms, *Science* **272**, 1325-1328 (1996).

[2] J. L. Cohn, G.S. Nolas, V. Fessatidis, T. H. Metcalf, G.A. Slack, *Phys. Rev. Lett*. **82**, 779 (1999).

[3] Q. Zeng, B. Sun, K. Du, W. Zhao, P. Yu, C. Zhu, J. Xia, Y. Chen, X. Cao, Q. Yan, Z. Shen, T. Yu, Y. Long, Y.K. Koh, Z. Liu, 2D Materials 6, 045009 (2019).

[4] S. Shimizu, J. Shiogai, N. Takemori, S. Sakai, H. Ikeda, R. Arita, T. Nojima, A. Tsukazaki, Y. Iwasa, Nature. Commu. 10, 825 (2019).

[5] J. Duan, X. Wang, X. Lai, G. Li, K. Watanabe, T. Taniguchi, M. Zebarjadi, E.V. Andrei, Proc. Natl. Acad. Sci. USA 113, 14272 (2016).

[6] Y. Xu, Z. Gan, S.-C. Zhang, *Phys. Rev. Lett*. **112**, 226801 (2014).

[7] S.Y. Matsushita, K.K. Huynh, H. Yoshino, N.H. Tu, Y. Tanabe, K. Tanigaki, Phys. Rev. Mater. 1, 054202 (2017).

[8] C.L. Kane, E.J. Mele, *Phys. Rev. Lett.* **95,** 146802 (2005)

[9] M.Z. Hasan, C.L. Kane, *Rev. Mod. Phys*. **82**, 3045-3067 (2010).

[10] K. Saha, I. Garate, Phys. Rev. B 90, 245418 (2014).

[11] K. Nomura, A.H. MacDonald, Phys. Rev. Lett. 98, 076602 (2007).

[12] K. Nomura, M. Koshino, S. Ryu, Phys. Rev. Lett. 99, 146806 (2007).

[13] P. Wei, W. Bao, Y. Pu, C.N. Lau, J. Shi, Phys. Rev. Lett. 102, 166808 (2009).

[14] Y.M. Zuev, W. Chang, P. Kim, Phys. Rev. Lett. 102, 096807 (2009).

[15] S.Y. Matsushita, K.K. Huynh, K. Tanigaki, Phys. Rev. B 99, 195302 (2019).

[16] J. Zhang, C.-Z. Chang, Z. Zhang, J. Wen, X. Feng, K. Li, M. Liu, K. He, L. Wang, X. Chen, Q.-K. Xue, X. Ma, Y. Wang, Nature Commun. 2, 574 (2011).

[17] S. Cho, B. Dellabetta, A. Yang, J. Schneeloch, Z. Xu, T. Valla, G. Gu, M. J. Gilbert, N. Mason, Nature Commun. 4, 1689 (2013).

[18] A.A. Taskin, Z. Ren, S. Sasaki, K. Segawa, Y. Ando, *Phys. Rev. Lett.* **107**, 016801 (2011).

[19] T. Arakane, T. Sato, S. Souma, K. Kosaka, K. Nakayama, M. Komatsu, T. Takahashi, Z. Ren, K. Segawa, Y. Ando, *Nature Commun*. **3**, 636 (2012).

[20] S.K. Kushwaha, I. Pletikosić, T. Liang, A. Gyenis, S.H. Lapidus, Y. Tian, H. Zhao, K.S. Burch, J. Lin, W. Wang, H. Ji, A.V. Fedorov, A. Yazdani, N.P. Ong, T. Valla, R.J. Cava, Nature Commu. 7, 11456 (2016).

[21] K. Ichimura, S.Y. Matsushita, K.K. Huynh, K. Tanigaki, Appl. Phys. Lett. 115, 052104 (2019).

[22] Y. Xu, I. Miotkowski, C. Liu, J. Tian, H. Nam, N. Alidoust, J. Hu, C.-K. Shih, Z. Hasan, Y.P. Chen, Nature. Phys. 10, 956 (2014).

[23] E.B. Kim, P. Dharmaiah, D. Shin, K.-H. Lee, S.-J. Hong, J. Alloys Compd. 703, 614 (2017).

[24] B. Huang, C. Lawrence, A. Gross, G.-S. Hwang, N. Ghafouri, S. W. Lee, H. Kim, C.-P. Li, C. Uher, K. Najafi, M. Kaviany, J. Appl. Phys. 104, 113710 (2008).

[25] D.-Y. Chung, T. Hogan, P. Brazis, M. R-. Lane, C. Kannewurf, M. Bastea, C. Uher, M.G. Kanatzidis, Science 287, 1024 (2000).

[26] M. Lee, L.Viciu, L. Li, Y. Wang, M.L. Foo, S. Watauchi, R.A. Pascal Jr, R.J. Cava, N.P. Ong, Nature Mater. 5, 537 (2006).

[27] J. Fukuyado, K. Narikiyo, M. Akaki, H. Kuwahara, T. Okuda, Phys. Rev. B 85, 075112 (2012).

[28] S. Shimizu, M.S. Bahramy, T. Iizuka, S. Ono, K. Miwa, Y. Tokura, Y. Iwasa, Proc. Natl. Acad. Sci. USA 113, 6438 (2016).

[29] M. Yoshida, T. Iizuka, Y. Saito, M. Onga, R. Suzuki, Y. Zhang, Y. Iwasa, S. Shimizu, Nano Lett., 16, 2061-2065 (2016).

[30] Y. Zhang, B. Feng, H. Hayashi, C.-P. Chang, Y.-M. Sheu, I. Tanaka, Y. Ikuhara, H. Ohta, Nat. Commun. 9, 2224 (2018).

[31] L.-D. Zhao, G. Tan, S. Hao, J. He, Y. Pei, H. Chi, H. Wang, S. Gong, H. Xu, V. P. Dravid, C. Uher, G.J. Snyder, C. Wolverton, M.G. Kanatzidis, Science 351, 141 (2016).

[32] K. Hippalgaonkar, Y. Wang, Y. Ye, D.Y. Qiu, H. Zhu, Y. Wang, J. Moore, S.G. Louie, X. Zhang, Phys. Rev. B 95, 115407 (2017).

[33] T. Chiba and A, Takahashi, J. Appl. Phys. 126, 245704 (2019).

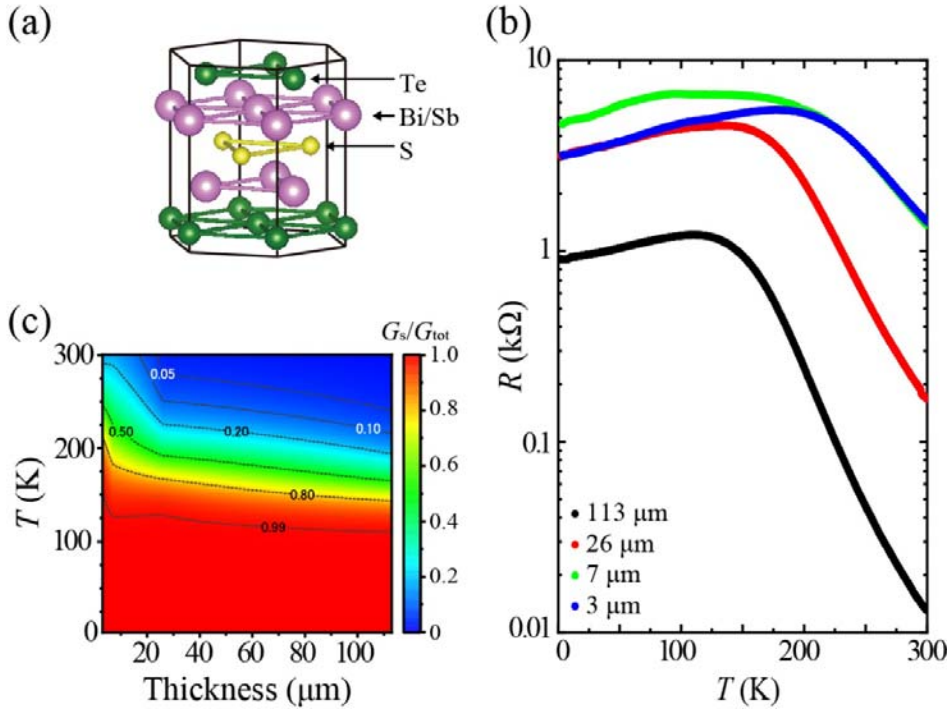

Figure 1. Crystal structure and electronic resistivity of Sn-BSTS flakes. (a) Crystal structure of Sn-BSTS. One quintuple layer (QL) has two sets of Te (green), Bi/Sb (pink) layers, and one S (yellow) layer at the center. The Sn atom is doped into the Bi/Sb layer (not shown in the figure). (b) Evolution of electronic sheet resistance as a function of T of four Sn-BSTS flakes with different thicknesses of 113, 26, 7, and 3 μm. (c) Colored contour map of surface dominant conductance (G_s/G_{tot}: the ratio of sheet conductance of the surface to the total sheet conductance) as a function of T and sample thickness. G_{tot} was calculated from the experimental sheet resistance R_{sh}, and G_s was estimated from the fitting analyses of sheet resistance, as described in the main text.

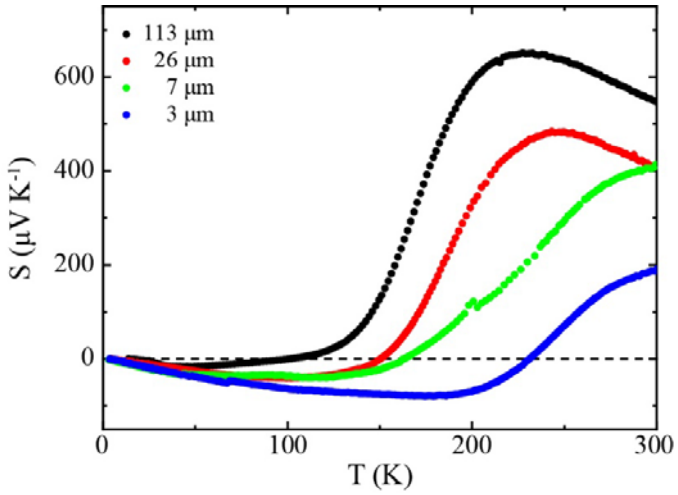

Figure 2. Thermopower (S) of Sn-BSTS flakes. Evolution of Thermopower (Seebeck coefficient) as a function of *T* of four Sn-BSTS flakes with different thicknesses of 113, 26, 7, and 3 μm.

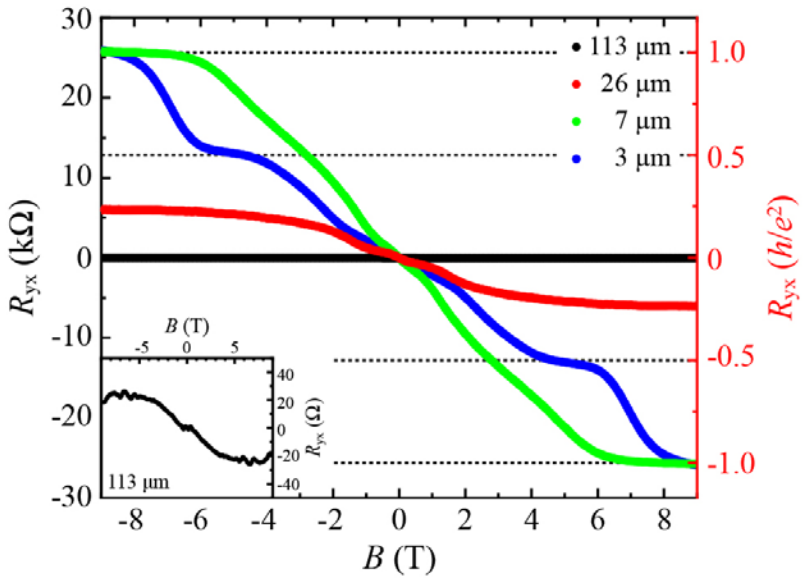

Figure 3. Hall resistance of Sn-BSTS flakes. Hall resistance of Sn-BSTS flakes of 113 μm-, 26 μm-, 7 μm-, and 3 μm-thicknesses at 2 K. The R_{yx} of the 7 μm-flake saturates at $R_{yx} = h/e^2$, and that of the 3 μm-flake shows plateaus at $R_{yx} = h/2e^2$ and $R_{yx} = h/e^2$ of QSHE in 3D-TIs. The inset is the enlarged view of the R_{yx} of the 113 μm-flake.

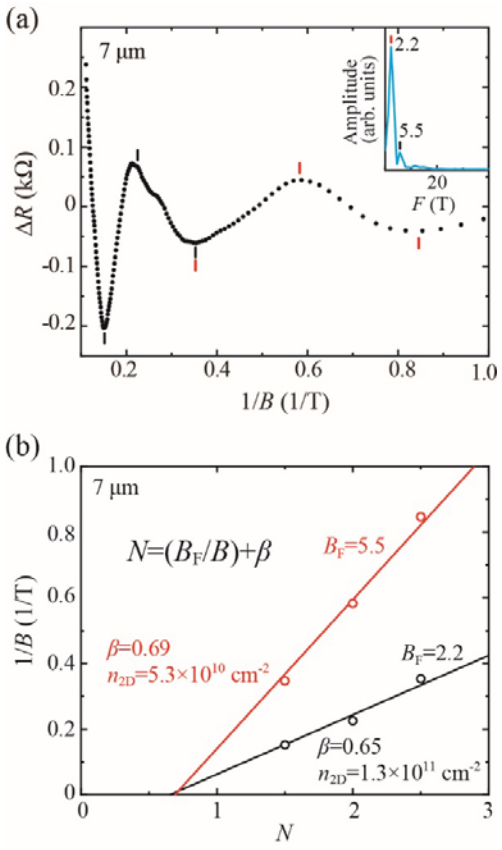

Figure 4. The Shubnikov-de-Haas (SdH) oscillations of 7 μm Sn-BSTS flake. (a) The SdH oscillations of 7 μm-flake. The inset is the FFT of the SdH oscillations. Two oscillation frequencies of 2.2 T (red bars) and 5.5 T (black bars) are detected. (b) Fan-diagram plots of the two SdH oscillations.

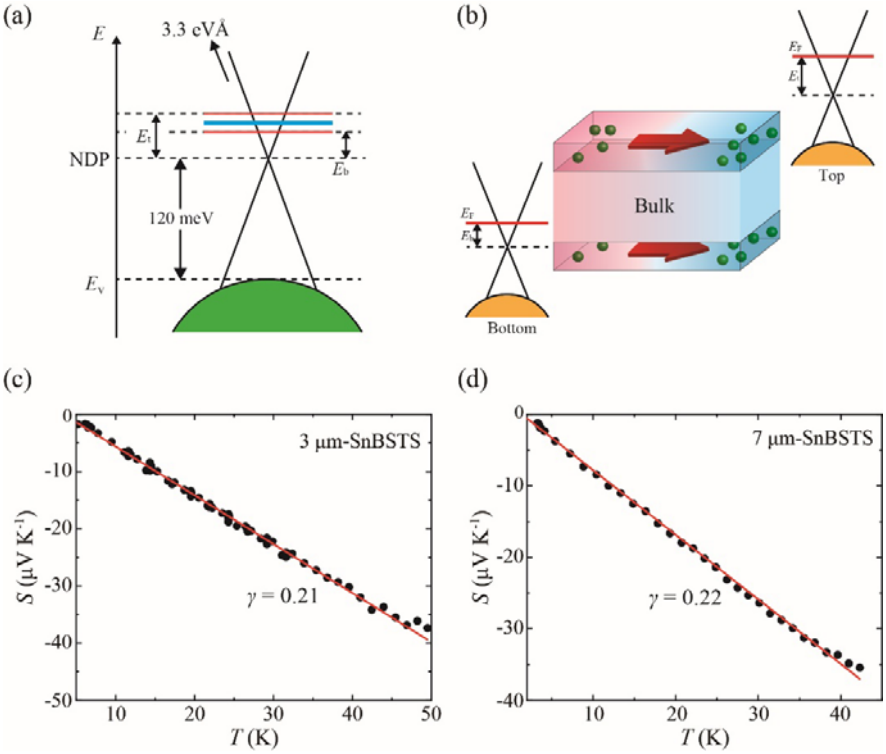

Figure 5. Intrinsic TE properties of TSDSs in Sn-BSTS. (a) A schematic band picture of the 3 μm- and the 7 μm- Sn-BSTS flakes calculated from analysis of the SdH oscillations. The position of E_F from the NDP of the top surface (E_t) is 44 meV for the 3 μm- and 40 meV for the 7 μm-flake, respectively. The E_F of the bottom surface (E_b) is 26 meV (red lines) for both flakes. The chemical potential of the bulk (blue line) is estimated as the average of the two TSDSs. (b) A schematic model of TE transport in 3D-TIs with a parallel circuit channel model. (c) and (d) Analytical fitting of thermopower (S) for the 3 μm- and 7 μm-flake, respectively.

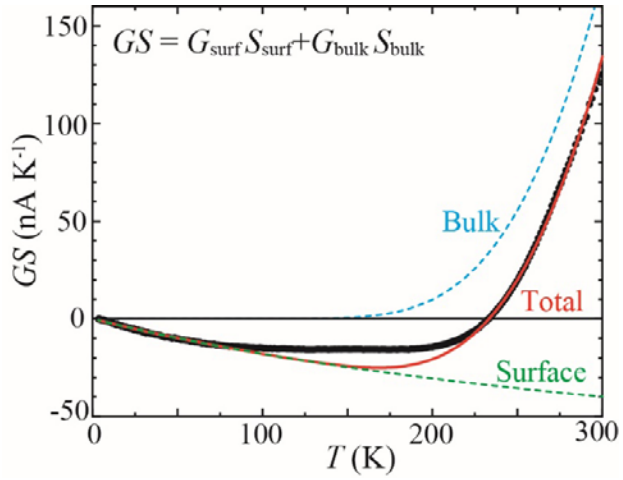

Figure 6. Deconvolution of GS between TSDSs and insulating bulk (iB). Each term of TSDS and iB was calculated based on the Boltzmann equations using the accurate band picture derived from the experimental results. The total GS values are almost identical to the experimental values.

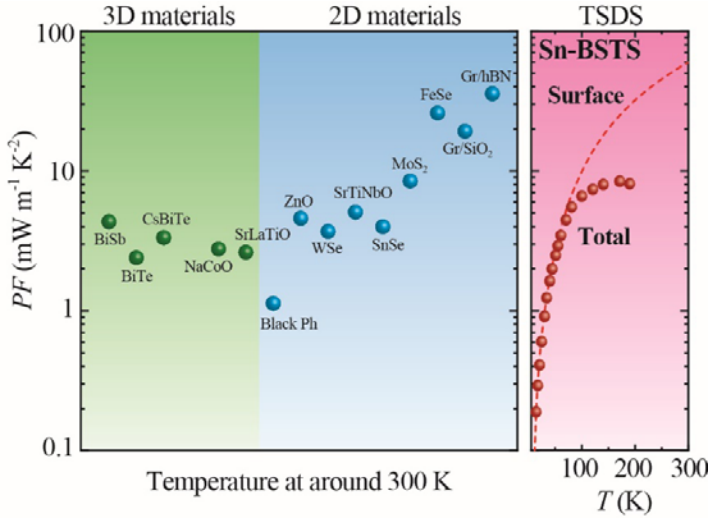

Figure 7. PF among 2D and 3D thermoelectric materials. PF values of 3D bulk crystals (green closed circles) at 300 K (ref. 23-27); PF values of the 2D material thin films (blue ball) (ref 3-5, and 28-32). PF of Sn-BSTS is plotted on the right side as a function of *T* (Red ball), which were calculated from the sheet resistance and Seebeck coefficient in Fig. 1. They increase with an increase in *T* below 80 K. The saturation above 80 K is caused by the contribution of the bulk carriers thermally excited at high *T*s. The red dashed line in the right panel represents the intrinsic PF values of pure TSDS of Sn-BSTS at high *T*s evaluated from the deconvolution analysis of GS shown in Fig.6 (details are described in the main text).

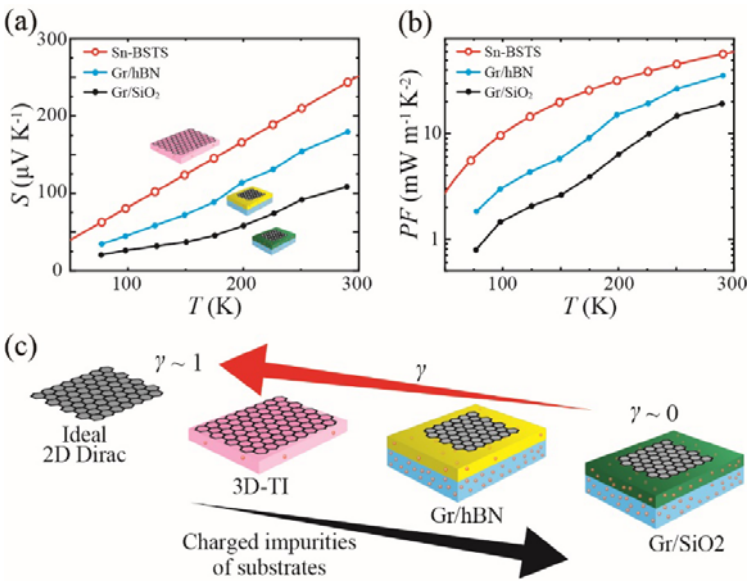

Figure 8. Comparison of TE properties on TSDSs: Sn-BSTS vs graphene. (a) Seebeck coefficients and (b) PFs of TSDSs on 3 μm Sn-BSTS and graphene/hBN. The solid line is the connection of the deconvoluted values for TSDSs (discussed in the text and shown in Fig. 3d). The experimental values of Gr/hBN (blue) and Gr/SiO_2 (black) are taken from ref. 5. (c) A schematic image showing structural features of the two Dirac systems of 3D-TI and Gr. Charged impurities of a substrate (red closed circles) perturbed fluctuations in the intrinsic Coulomb scattering potential, which decreases γ to suppress the enhancement in S and PF of Dirac-electron states.